

# Direct Correlation of Single-Particle Motion to Amorphous Microstructural Components of Semicrystalline Poly(ethylene oxide) Electrolytic Films

Trevor D. Roberts,<sup>#</sup> Rongfeng Yuan,<sup>#</sup> Limin Xiang, Milan Delor, Ravi Pokhrel, Ke Yang, Emad Aqad, Tomas Marangoni, Peter Trefonas, Ke Xu, and Naomi S. Ginsberg\*

**Cite This:** *J. Phys. Chem. Lett.* 2020, 11, 4849–4858

**Read Online**

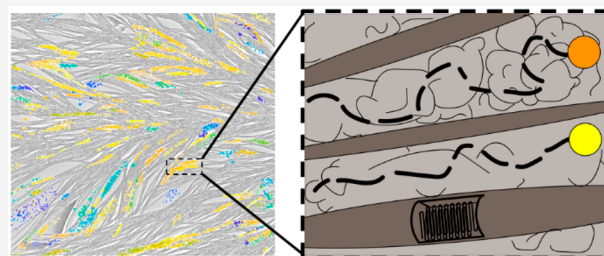
ACCESS |

Metrics & More

Article Recommendations

Supporting Information

**ABSTRACT:** Semicrystalline polymers constitute some of the most widely used materials in the world, and their functional properties are intimately connected to their structure on a range of length scales. Many of these properties depend on the micro- and nanoscale heterogeneous distribution of crystalline and amorphous phases, but this renders the interpretation of ensemble averaged measurements challenging. We use superlocalized widefield single-particle tracking in conjunction with AFM phase imaging to correlate the crystalline morphology of lithium-triflate-doped poly(ethylene oxide) thin films to the motion of individual fluorescent probes at the nanoscale. The results demonstrate that probe motion is intrinsically isotropic in amorphous regions and that, without altering this intrinsic diffusivity, closely spaced, often parallel, crystallite fibers anisotropically constrain probe motion along intercalating amorphous channels. This constraint is emphasized by the agreement between crystallite and anisotropic probe trajectory orientations. This constraint is also emphasized by the extent of the trajectory confinement correlated to the width of the measured gaps between adjacent crystallites. This study illustrates with direct nanoscale correlations how controlled and periodic arrangement of crystalline domains is a promising design principle for mass transport in semicrystalline polymer materials without compromising their mechanical stability.



Solution processable semicrystalline polymers, such as polyethylene and its derivatives<sup>1</sup> as well as numerous nylons and rubbers,<sup>2</sup> are an important class of materials and constitute one of the largest groups of commercially useful polymers. Intimately connected to the polymer's functional properties are the morphologies<sup>3–6</sup> resulting from various means of preparation, wherein the distribution of crystalline and amorphous material is inhomogeneous on a wide variety of length scales.<sup>7–9</sup> Crystallinity in such materials typically corresponds to greater mechanical strength but renders the material more brittle, and more amorphous character corresponds to greater flexibility at the cost of mechanical strength.<sup>10</sup> It is well-known that the polymer material is more fluid in its amorphous state and more rigid in the crystalline state, as lamellar crystallites form when polymer chains tightly fold upon themselves, which increases local material density and reduces free volume.<sup>11–13</sup> Additionally, when doped with ionic salts, some polymers can form ordered polymer–ion crystalline complexes, where the polymer chain backbone tightly coordinates around charged ions, as has been demonstrated for poly(ethylene oxide) (PEO).<sup>14–20</sup> It is generally believed that crystallites behave as impermeable boundaries for the transport of ions, molecules, and other dopants in the amorphous state.<sup>21–24</sup> PEO is a particularly

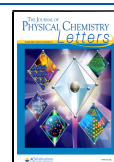
well-studied semicrystalline polymer with applications for solid-state electrolytes, for example, in batteries.<sup>25</sup> As ambient temperature is between the range of glass transition temperatures ( $\sim -67$  to  $-28$  °C) and melting temperatures ( $\sim 55$  to  $65$  °C) of PEO, it offers desirable transport properties for ions as well as desirable structural integrity for incorporation in devices and for Li dendrite suppression. Room temperature ion conductivity remains to be improved, however, and strategies to improve conductivity generally involve suppressing crystallinity, which is typically monitored as a fractional composition in bulk.<sup>26–29</sup>

Unfortunately, despite the heterogeneous morphology of semicrystalline polymer materials like PEO, most measurements of material parameters are made in bulk,<sup>14,19,25,30–35</sup> making it challenging to associate specific elements of the morphology with functional attributes. For example, bulk

**Received:** April 30, 2020

**Accepted:** May 26, 2020

**Published:** June 8, 2020



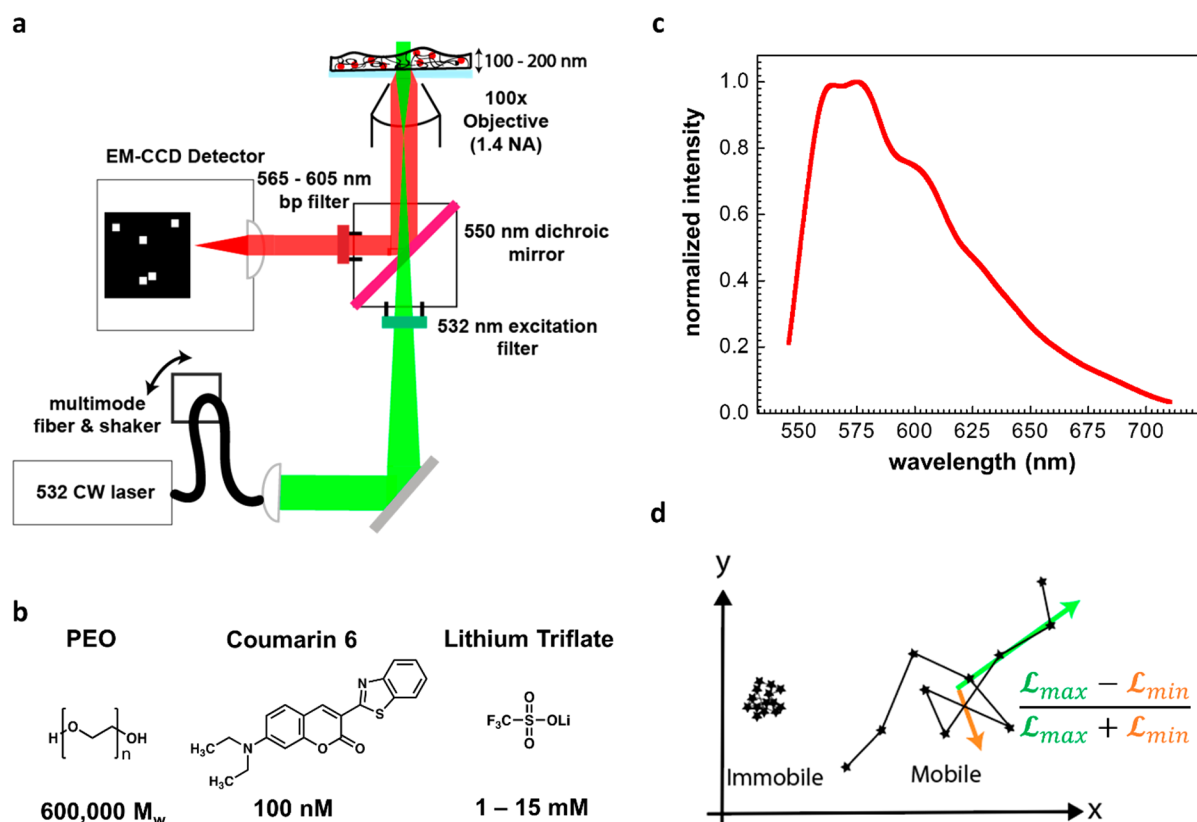


**Figure 1.** Single-particle tracking of Coumarin 6 fluorescent probe complexes in poly(ethylene oxide) (PEO) thin films codoped with lithium triflate (LiOTf). (a) Schematic of single-particle fluorescence imaging, with 532 nm continuous wave excitation of thin-film sample and emission detection between 565 and 605 nm. The laser output is coupled through a multimode fiber to scramble its polarization and is shaken at a sufficient frequency to spatially average the intensity pattern in each frame. The 532 nm beam is then passed through a 532 nm excitation filter and 550 nm dichroic mirror before arriving at the objective. (b) PEO (600 000  $M_w$ ) is dissolved along with 100 nM Coumarin 6 and 1–15 mM LiOTf. (c) Average of over 200 000 single-particle spectra of 10 mM LiOTf and 100 nM C6 codoped PEO thin film, using 532 nm excitation. (Spectra acquired on separate, spectrally resolved single-molecule fluorescence microscope.) See also Figure S1. (d) Schematic of immobile and mobile particle trajectories, with the major principal component of the mobile trajectory shown in green and the minor principal component shown in orange. The anisotropy parameter is defined as the difference between the maximum eigenvalue and minimum eigenvalue divided by the sum of the maximum and minimum eigenvalues generated by principal component analysis.

conductivity measurements average the motion of ions over length scales orders of magnitude larger than the separation between crystalline and amorphous phases. A more explicit measurement of how small species—whether charged or neutral—move as a function of the film microstructural components could help to more explicitly identify optimal morphologies that balance mechanical and transport properties. By characterizing the motion of a neutral probe specifically as a function of nanoscale spatial coordinates and morphological composition, we stand to gain more insight into precisely how crystallites influence transport. Furthermore, a nanoscale mapped correspondence between morphological composition and motion of a probe would demonstrate whether probe motion in amorphous regions is affected by region size and proximity to crystallites.

Here, we therefore correlate the mechanical and morphological spatial map of a semicrystalline polymer via atomic force microscopy (AFM) phase imaging with single-particle localization and dynamic tracking (SPT) to map the motion of a probe in films as a function of composition and resulting morphology. Previous studies correlating AFM with fluorescence imaging demonstrate how the two characterizations can complement one another<sup>36,37</sup> and even elucidate discrepancies<sup>38</sup> between the two imaging modalities. We use

a ternary system of PEO, lithium triflate (LiOTf), and fluorescent Coumarin 6 (C6) to measure the nanoscale motion of fluorescent C6 complexes at 40 nm precision and correlate it to film morphology obtained via AFM phase imaging. We observe that crystallites generally behave as impermeable barriers for probe transport and anisotropically constrain the transport of probes along intercalating amorphous channels. Furthermore, we observe that the probe diffusion coefficients along the major axis of travel for both isotropic (amorphous) and anisotropic (crystallite-rich) probe trajectories are the same. This correlation between morphology and probe diffusion suggests that AFM phase images can be used to predict probe transport and that SPT is a faithful reporter of semicrystalline morphology.

**Experimental Method.** To investigate the role crystallinity plays in dictating probe motion, we prepare spin-coated thin film ( $\sim 100$  nm) consisting of 600 000  $M_w$  PEO, LiOTf, and C6. These samples serve as model semicrystalline polymer systems, as the LiOTf is present at relevant millimolar (mM) concentrations, and C6 is present at much lower nM concentrations (Figure 1b and see below). LiOTf is a common lithium salt used in Li-ion battery research,<sup>25</sup> and we use the doping concentration of LiOTf to tune the relative crystallinity and corresponding morphology of the system at room

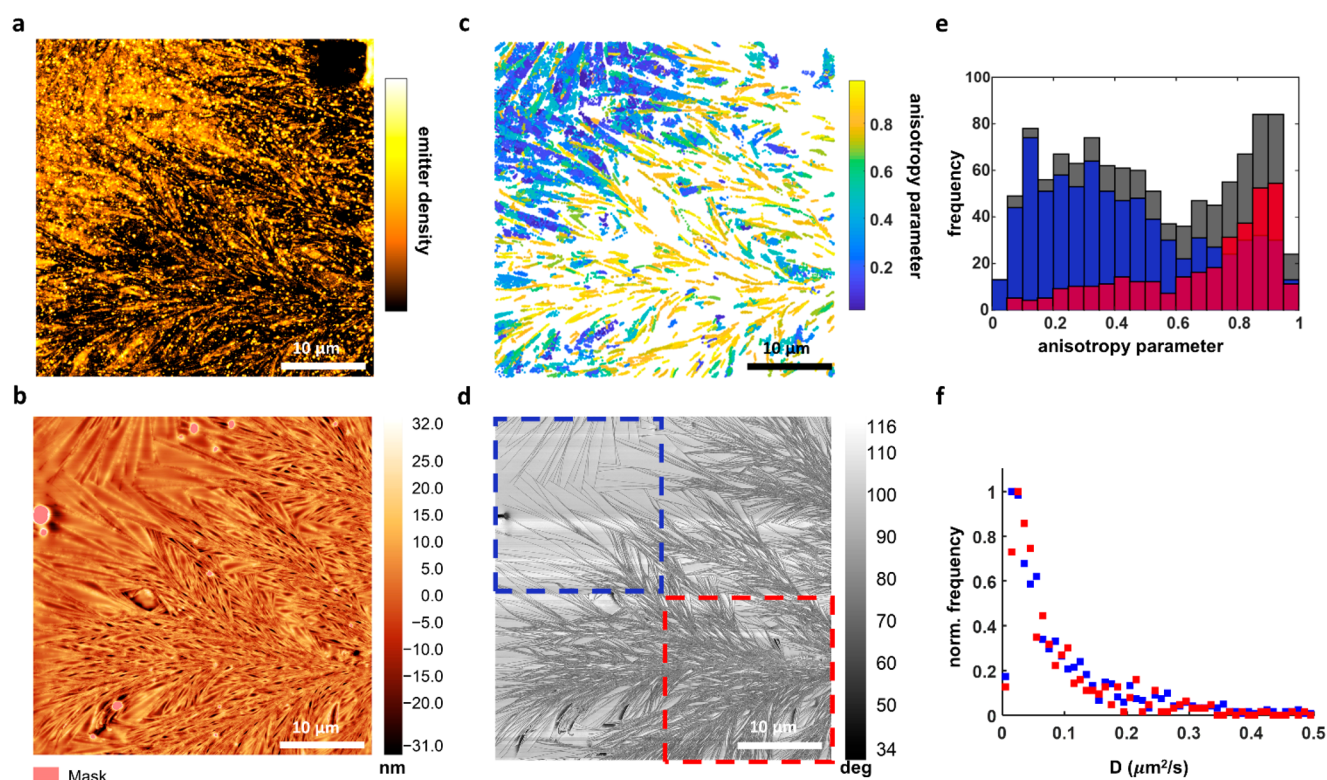


**Figure 2.** Correlative single-particle tracking and AFM imaging. (a) Superlocalized fluorescence image with superimposed 2D Gaussian fits to individual Coumarin 6 aggregates integrated over 8000 frames with 100 ms of exposure per frame. The size of each point corresponds to the precision of fit of the emitter position. The false-color intensity at a given location is proportional to the density of emitters detected at that location. (b) Tapping-mode AFM height image in same region of interest as (a). Light red coloring corresponds to masked-off regions not included in height range of  $-31$  to  $32$  nm. (c) Plot of trajectories that sampled greater than 15 frames and with diffusion coefficients greater than  $0.0075 \mu\text{m}^2/\text{s}$ . Trajectories are color-coded by anisotropy parameter, with blue colors corresponding to isotropic trajectories and yellow colors corresponding to most anisotropic trajectories. (d) Tapping-mode AFM phase image of same ROI as (b). Crystallites are darker contrast rods, while amorphous material is lighter and featureless in between and outside of crystallites. (e) Distribution of anisotropy parameters of mobile trajectories corresponding to red and blue squares in (d). The blue distribution corresponds to trajectories within the blue square; the red distribution includes trajectories found within the red square. The gray distribution is the sum of the distributions from the blue and red regions. (f) Normalized distribution of 1D diffusion coefficients along the major axes of trajectories. Blue data points correspond to the distribution of trajectories within the blue square in (d); red data points correspond to the distribution of trajectories within the red square in (d). While values beyond  $0.5 \mu\text{m}^2/\text{s}$  were also measured, only the range from 0 to  $0.5 \mu\text{m}^2/\text{s}$  is plotted for clarity.

temperature. According to the phase diagram describing the PEO–LiOTf system,<sup>26,39</sup> at 15 mM LiOTf doping, crystallites are likely PEO:LiOTf crystalline complexes, and a significant amorphous component is also present possibly due to incomplete crystallization.<sup>33</sup> C6 is hydrophobic and forms fluorescent aggregates with red-shifted absorption and emission spectra in polar media,<sup>40,41</sup> which we use as robust fluorescent probes that enable multiframe particle tracking and localization (Figures 1a and S1). By exciting at 532 nm, we selectively follow these red-shifted aggregates.

Additional spectrally resolved single-molecule fluorescence microscopy measurements<sup>42,43</sup> (Figure 1c) confirm that the probes in films also containing LiOTf are not individual C6 molecules red-shifted as a consequence of direct proton interaction, a known interaction of C6<sup>44,45</sup> (Figure S1). The nature of the probe is further substantiated by the averaged single-particle spectrum, which shows much broader features than unprotonated or protonated individual C6 molecules. Furthermore, the average probe emission spectrum is not correlated to particle mobility and does not depend on the identity of the salt cation (Figure S1). The averaged probe spectrum shows a minor, if any, dependence on the concentration of salt (Figure S1), yet increasing the LiOTf

concentration markedly increases the C6 aggregate fluorescence from a film (Figure S2). To this end, we find that for a fixed C6 concentration, the number of single fluorescent aggregate particles detected per imaging frame is linearly proportional to the salt concentration (Figure S3). Overall, these findings suggest that the probes are LiOTf-induced C6 aggregates.

We use widefield single-particle tracking (SPT) to explain how morphological heterogeneities on the order of tens of nm influence probe motion, which has also proven to be useful in deducing nanoscale behavior in a variety of biological,<sup>46–48</sup> polymer,<sup>49–55</sup> and other material<sup>56</sup> systems. We acquire movies with 100 ms of exposure ( $\sim 130$  ms frame-to-frame time) on an electron multiplying charge coupled device (EMCCD) camera with micromanager software<sup>57</sup> using continuous wave (CW) 532 nm illumination. Individual probes can then be followed over an average of 24 frames in order to learn how they explore the film morphology. Probe superlocalization is performed using the ImageJ GDSC SMLM plug-in,<sup>58</sup> and trajectories are reconstructed using MATLAB scripts. The average localization precision of particles is  $\sim 40$  nm, and the distribution of particles and corresponding measured signal is shown in Figure S4. A representative image in Figure 2a is

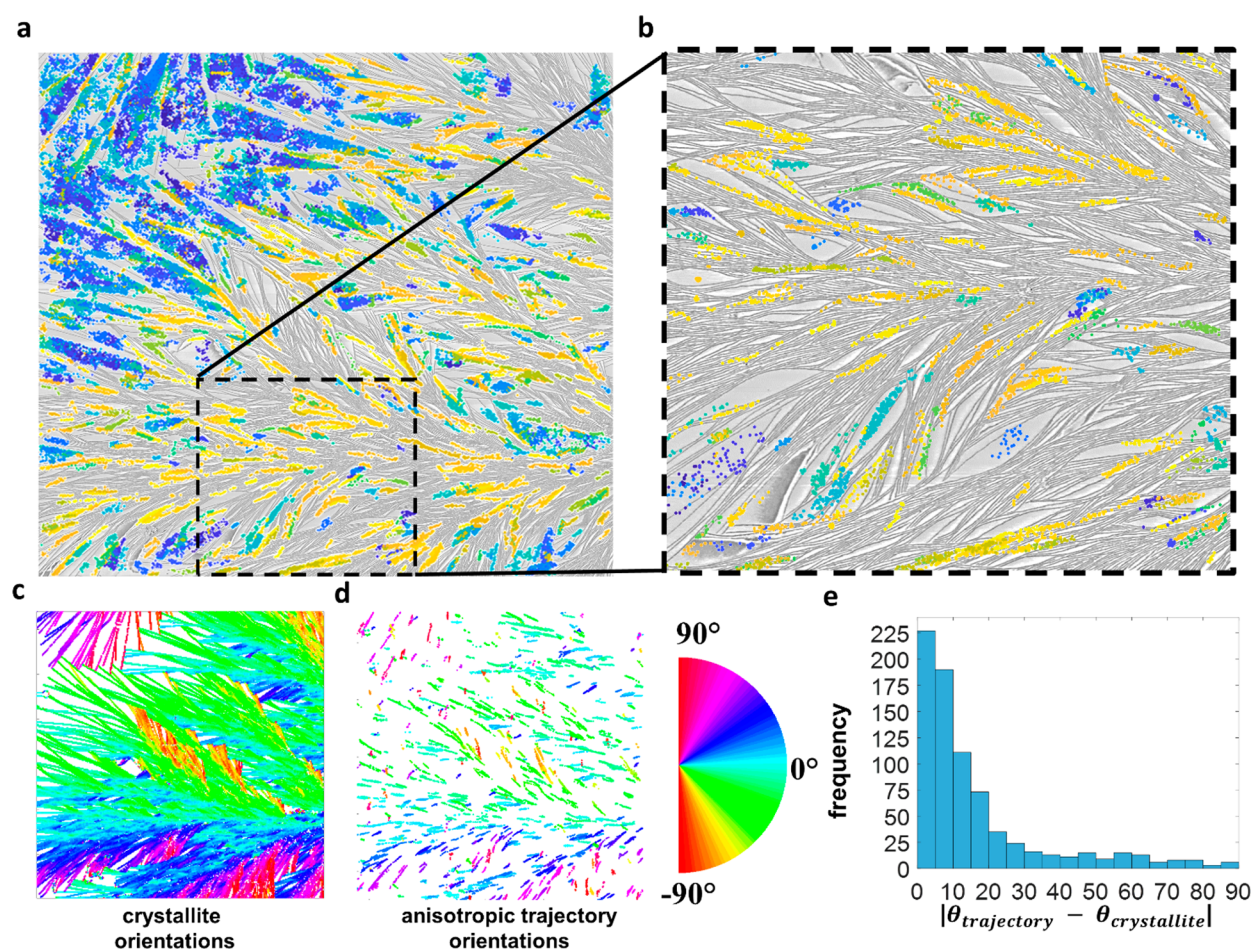


**Figure 3.** Overlay of mobile trajectories color-coded by anisotropy parameter with AFM phase image. (a) Full,  $40 \times 40 \mu\text{m}^2$ , field of view of Figure 2c,d. (b) Magnification of  $15 \times 15 \mu\text{m}^2$  dashed box in (a). Each colored point in panels (a) and (b) corresponds to the location of a distinct detected individual emitter. (c) Pixel-binned and binarized  $40 \times 40 \mu\text{m}^2$  AFM phase image from Figure 2d, where each pixel is color-coded according to the semicircle inset and corresponds to the average orientation of crystallites relative to the lab frame horizontal. (d) Probe trajectories from the same  $40 \times 40 \mu\text{m}^2$  ROI as (c) possessing an anisotropy parameter greater than 0.75 with each step of each trajectory color-coded by the orientation of a trajectory's major axis relative to the lab frame horizontal. (e) Distribution of values corresponding to the difference between a trajectory's major axis orientation and the crystallite orientation in the location of the trajectory's average position.

generated by fitting each emitter in each frame to a 2D Gaussian and then superimposing the collection of all Gaussian fits. The width of each spot represents the localization error, and the intensity represents the density of distinct emitters found within the spot. The mean squared displacement (MSD) of each trajectory thus identified is obtained using a two-dimensional Brownian diffusion model. We characterize the anisotropy of probe trajectories using principal component analysis (PCA) on vectors that represent each step and are repositioned to originate at the origin of the coordinate system. Major and minor axes, along with their respective variances,  $L_{\text{max}}$  and  $L_{\text{min}}$ , are extracted. We define the anisotropy parameter of a trajectory to be  $(L_{\text{max}} - L_{\text{min}}) / (L_{\text{max}} + L_{\text{min}})$  (Figure 1d). In our analysis, we consider only trajectories of probes that we take to be *mobile*, i.e., whose diffusion coefficients are above a threshold of  $0.0075 \mu\text{m}^2/\text{s}$ .

To correlate the dynamical single-particle trajectory data (Figure 2a,c) to specific microstructural components of the films, we correlate it to tapping-mode AFM phase images (Figure 2b,d). To ensure the same fields of view are imaged with the two different techniques, the AFM measurements are first performed on a particular  $40$  by  $40 \mu\text{m}$  region of interest (ROI), and then, the single-particle tracking can be done on

the same ROI through the use of a fiducial marker created in the AFM (see Supporting Information (SI) methods). Using a tip radius  $< 10$  nm, we deduce regions of amorphous and crystalline character on relevant tens of nm length scales.

**Results.** Comparing dynamical and structural information within the same field of view enables a variety of important correlations to be established. The superlocalized fluorescence image of the SPT data (Figure 2a) provides a representation of trajectories obtained in a given movie recording, where the false-color intensity indicates the emitter density. There is a higher density of emitters in the top left as compared to the bottom left of the frame. Furthermore, thin, elongated patterns can be identified on the right-hand side of the image, whereas no such patterns are apparent in the top left of the frame. The AFM height map used to prepare Figure 2b has an original height range of  $-78$  to  $523$  nm, and this large range is due to some very tall continuous structures identified with red overlay. Upon thresholding to remove these structures, the image height variation becomes limited to  $-31$  to  $32$  nm. The AFM phase image in Figure 2d has a range of  $82^\circ$  and is marked by a series of thin, rod-like shapes at a lower phase angle (darker) than the uniform background (lighter), and these shapes agree with other AFM phase images of

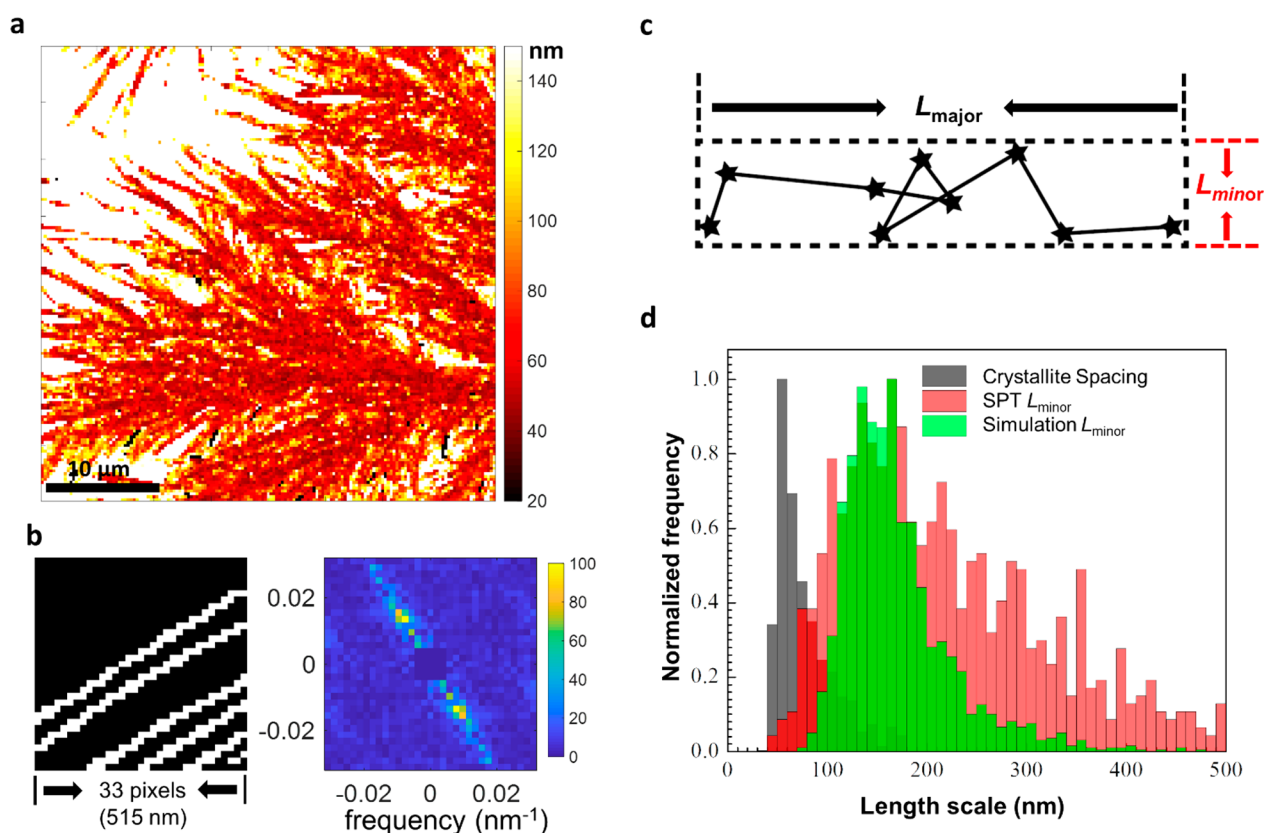


**Figure 4.** Comparison of crystallite spacing to trajectory width. (a) A heat map of crystallite spacing extracted from the AFM phase image (Figures 2 and 3) using a 2D FFT. The method is illustrated in (b). The left black and white image is a cropped, binarized AFM phase image, in which the black and white regions correspond to amorphous and crystallite regions, respectively. The width of this binarized ROI is 515 nm ( $33 \times 15.6$  nm pixel size), corresponding to a very small point in (a). Its 2D FFT generates the heat map of spatial frequency (at right). Yellow corresponds to high amplitude, while deep blue means low amplitude. We report the local crystallite spacing in the false color of (a) as described in the SI additional methods. The average crystallite spacing that can be extracted in this example is 64 nm. (c) Schematic to illustrate definition of the minor axis width (red) of a trajectory (black stars connected by solid black lines), as compared to the major axis width (black). (d) The distribution of crystallite spacing obtained from 2D FFT analysis is shown in black. Spacings above 150 nm are not included due to the ROI size. The distribution of trajectory widths on the minor axis for anisotropic trajectories (anisotropy parameter  $> 0.75$ ) is shown in red. The distribution of trajectory widths of simulated trajectories that sample confinement from the black distribution of crystallite spacings and a localization error from a 40 nm Gaussian distribution is shown in green.

semicrystalline PEO.<sup>59–62</sup> Figure 2c plots the trajectories of fluorescent probe centroids obtained from Figure 2a, color-coded by the anisotropy parameter defined in Figure 1d. Blue colors represent the most isotropic trajectories (approaching 0), yellow colors represent the most anisotropic trajectories (approaching 1), and green colors represent intermediate values of the anisotropy parameter. Only trajectories of emitters that fluoresced for at least 15 consecutive frames and for which the diffusion coefficient  $D > 0.0075 \mu\text{m}^2/\text{s}$  are shown. Like in Figure 2a, the trajectories in the bottom right in this representation also show more rod-like shapes.

The dynamical data can be further represented by statistically characterizing the distributions of anisotropy parameters and diffusion coefficients associated with each trajectory within various subregions of the ROI in Figure 2a–d. The gray histogram in Figure 2e shows the total distribution of anisotropy parameters for all trajectories found in both boxed regions in Figure 2d. The red distribution presented over top of it includes the anisotropy parameters for trajectories only in the red box in Figure 2d, and the blue distribution includes the anisotropy parameters for trajectories only in blue box. The red distribution is skewed much more toward a high anisotropy parameter, peaking at 0.95, and the

blue distribution is broadly isotropic, peaking at 0.15. In Figure 2f, we also compare distributions of trajectory diffusion coefficients for each of the boxed regions in Figure 2d. To obtain each of the diffusion coefficients, each step of a trajectory is first projected along the major axis of motion determined by PCA, and a diffusion coefficient is computed by equating the mean squared displacement of these projected steps to  $2Dt$ , for diffusion coefficient  $D$  and trajectory duration  $t$ . This procedure is employed for both isotropic and anisotropic trajectories in order to compare them using a common metric. Interestingly, both the data from the blue and red regions in Figure 2d have similar distributions of diffusion coefficients. Both distributions peak near  $0.03 \mu\text{m}^2/\text{s}$  and tail off at  $0.4 \mu\text{m}^2/\text{s}$ .

We next relate the AFM and SPT data in Figure 2 to compare and contrast crystallite-rich and amorphous-rich regions. The bottom right corner of the ROI in Figure 2a–d corresponds to a PEO crystallite-rich region where anisotropic probe trajectories are most common. The directionality of the crystallites appears to be imprinted onto the probe trajectories as well. In contrast, the top left corner of the ROI is primarily composed of amorphous material and probe trajectories there are mostly isotropic in nature. Even within regions of dense

crystallites,  $\sim 1\text{--}2\ \mu\text{m}^2$  pockets of amorphous polymer yield isotropic trajectories (more isolated blue spots in Figure 2c). We find similar results upon repeating the correlative AFM and SPT experiments in additional films independently prepared with the same composition (Figure S5). The distribution of major axis diffusion coefficients for both primarily amorphous and primarily crystalline regions are very similar, suggesting that probe trajectories in crystallite-rich regions are unhindered along the direction of crystalline fibers. In addition to the peak anisotropy parameter values, the blue and red distributions in Figure 2e each have a substantial spread. We simulated isotropic and anisotropic random walks of various trajectory step lengths and confirmed that the spreads are primarily a consequence of a finite trajectory length (Figure S6), suggesting that the values at which the distributions each peak are more representative of the probe motion than the spreads.

To compare SPT trajectories and AFM-derived morphology more directly, we overlaid the data for Figure 2c,d in Figure 3a,b. The overlay shows that the majority of locations where the probes are observed fall within lighter contrast regions of the AFM data, which we take to represent amorphous PEO. In fact, the trajectories generally conform to the boundaries delineated by crystalline fibers, even when these fibers are curved. Generally, trajectories residing in more narrow channels between crystalline fibers are more anisotropic (yellow), and trajectories residing in larger pockets of amorphous material between crystallites are more isotropic (bluer). Exceptions to these categorizations could be due to out-of-plane amorphous channels crossing beneath the surface structure that we primarily map with AFM, though these exceptions are a small minority. Based on the similarity of the amorphous channel depth (up to 60 nm, Figure 2b) and film thickness ( $\sim 100$  nm), the similarity of major axis probe diffusivities measured in confined amorphous PEO and in unconfined regions as well as the comparable diffusivities observed in annealed PEO films (Figure S7), we infer that the probes diffuse within, as opposed to on the surface of, the amorphous PEO. In any case, the absence of isotropic trajectories in the crystallite-rich region remains as strong evidence for the structural/dynamical correlation.

Additional information regarding the extent to which crystalline fibers constrain probe motion can be obtained by further quantitating the degree of correlation between the crystallite boundary orientation and the major axes of nearby probe trajectories, which we do in Figure 3c–e. Figure 3c shows a color-coded map of crystallite orientations obtained by thresholding and binarizing the AFM phase image shown in Figures 2d and 3a (see Figure S8 for more detail). Similarly, Figure 3d shows a map using the same orientational color-coding for the major axis of tracked probe trajectories shown in Figures 2c and 3a, possessing an anisotropy parameter greater than 0.75. Visually, there is a high degree of spatial correlation between the structural and dynamical orientational maps in Figure 3c,d. To further quantify this correlation, Figure 3e shows the distribution of orientational mismatch between proximal crystallites and anisotropic probe trajectory major axis orientations,  $|\theta_{\text{trajectory}} - \theta_{\text{crystallite}}|$ . The distribution is peaked around zero mismatch with a half-width of  $\sim 15^\circ$ . This half-width is within the error of the average crystallite spacing calculated in Figure 4.

In addition to quantitating the orientational correlation between structural and dynamical information, we investigate

the correlations of spatial scales in our two types of measurements that relate to the apparent confinement of dynamical trajectories within narrow channels between crystalline fibers (Figure 4). To do so, we first perform a 2D fast Fourier transform (FFT) on the same thresholded and binarized AFM phase image as in our orientational analysis (Figure S8). Each pixel in Figure 4a is color-coded to represent the local period of, or spacing between, adjacent crystalline fibers, as calculated using the Fourier transform. To create this map, the 2D FFT is performed in spatial bins of 33 by 33 pixels, and the spatial bin is scanned over the thresholded, binarized image in steps of 16 pixels (Figure 4b). The distribution of spacings in Figure 4a is shown in Figure 4d (black) and ranges from 40 to 150 nm, peaking at 50–55 nm. Spatial periods larger than 150 nm are not reported on account of the size of spatial bins in the 2D FFT (see SI methods).

We next relate the spacings between crystallite fibers to the spatial extent of confined probe trajectories measured via SPT. For each trajectory possessing an anisotropy parameter value greater than 0.75, we consider the greatest distance between trajectory particle positions along the minor axis, as reported by PCA (schematic shown in Figure 4c). This minor axis width distribution peaks at 150 nm (Figure 4d, red). To reconcile this difference between the distribution of crystallite spacings reported by the 2D FFT analysis of the AFM phase image and the distribution of trajectory widths along the minor axis, we numerically simulate confined random walk trajectories. Each simulated trajectory is 29 frames long (median number of frames for anisotropic trajectories), and the degree of confinement for a given trajectory is drawn from the distribution of crystallite spacings extracted from AFM (Figure 4d, black). Furthermore, a random error drawn from a Gaussian distribution ( $\sigma = 40$  nm) is added to each position of a given trajectory to incorporate the effect of the 40 nm experimental localization error. The minor axis width distribution of these simulated trajectories is shown in Figure 4d in green and peaks at  $\sim 150$  nm. These simulations suggest that to within the 40 nm localization uncertainty of our SPT measurements, the peak trajectory minor axis width of 150 nm is consistent with the crystallite fiber spacing of 50–55 nm determined via FFT analysis (supported by simulations shown in Figure S9). Additional confined random walk simulations described in Figure S9 recapitulate this assertion. They show that a 40 nm localization uncertainty precludes using our SPT to discern 50 nm spacings between crystallite fibers from larger spacings unless these larger spacings are equal to or exceed 150 nm.

**Discussion.** The above results present an opportunity to further establish relationships between probe motion within semicrystalline PEO and its structural features. The discussion below focuses on the influence of the configuration and shape of crystallites on probe motion and on suggestions for how these findings serve as design principles for controlling crystalline growth within semicrystalline polymers. We consider the collection of our observations and analysis of location, orientation, and length scale correlations between the semicrystalline morphology map obtained by AFM and the probe motion within this morphology obtained by SPT.

Comparing the *locations* where the probes are observed to the locations of crystalline and amorphous components of the PEO film microstructure in the overlays in Figure 3 allowed us to establish that the probes are forced out of crystalline regions. This segregation is a probable result of the

crystallization process, as crystallization often purifies the material composition, forcing out impurities, such as the fluorescent probes. We also learned that the motion of the fluorescent probes within the amorphous PEO where they reside is isotropic, provided that the extent of the amorphous region exceeds a typical diffusion length of the probe. If, however, the extent of an amorphous region is smaller than the intrinsic diffusion length of the probes along a given axis, then the probe motion is confined along that axis, generating anisotropy in the probe trajectory. Incidentally, we also found that measuring single-particle trajectories in a given film before and after removing its crystalline microstructure via thermal annealing shifts the original anisotropy parameter distribution to become substantially more isotropic, while preserving the value of the unconfined diffusion coefficient (Figure S7).

The orientation of these anisotropic trajectories correlates strongly to the orientation of the crystalline boundaries, and the extent of this anisotropy is directly correlated to the extent of confinement between adjacent crystallites, which are often parallel to one another. Furthermore, the width of probe trajectories on the minor axis and its nearby crystallite spacing agree in size to within the uncertainty of our measurements. Though quantitatively correlating the extent of confined probe trajectories and the widths of amorphous channels beneath the SPT localization uncertainty of 40 nm is not currently possible, the degree of probe trajectory anisotropy is able to report on the specific spatial configurations of crystallites in the film morphology. In fact, the most extreme case of anisotropic probe motion is achieved by lowering the LiOTf concentration from 15 to 1 mM, which creates more densely packed, presumably pure PEO, crystallites configured in a spherulitic morphology, as compared to ones we primarily study in this work composed of a PEO–salt complex.<sup>39</sup> While PEO–salt crystallites and pure PEO crystallites differ in height, width, and spacing, it is interesting to note that both appear to behave functionally as impermeable barriers that geometrically confine the probe transport. Beyond this important similarity, the spherulite structures yield the most strongly anisotropic distribution of trajectories (Figure S10), and the amorphous channels between crystallite fibers traced by the fluorescent probes appear to be even thinner than in the case that we explored in detail in Figure S9. Our findings therefore suggest that the degree of anisotropy observed in fluorescent probe motion in SPT is an excellent reporter for lamellar crystallinity and that the semicrystalline microstructures observed in AFM phase images also report well on each of the location, confinement, and trajectory orientation of particle motion. This deduction is also well-supported by bulk conductivity measurements reported by Li and co-workers<sup>22</sup> that show ions preferentially travel parallel, and not perpendicular, to crystalline plates of PEO.

Our results suggest that PEO crystallites anisotropically constrain and guide probe motion but do not affect their diffusivity. This finding indicates that pursuit of a controlled arrangement of crystallites could be quite worthwhile for material design. Interestingly, such design strategies have been discussed in the context of semicrystalline semiconducting polymers, wherein charge transport actually occurs predominantly in crystalline domains, and intercrystallite transport can behave as a bottleneck.<sup>63,64</sup> In the case of ion motion in solid-state electrolytes, suppressing crystallinity has historically been the strategy to improve ion mobility, with the drawback of compromised mechanical strength. Rather than an exclusively

negative property for transport, if aligned and ordered, crystalline domains could serve as channel boundaries to deterministically guide dopant transport, a concept that has only recently begun to be explored.<sup>21,28</sup> In fact, Li and co-workers demonstrated that manufacturing single-crystalline plates of PEO can be used to anisotropically improve conductivity between plates.<sup>22</sup> We show here that spontaneously formed crystalline structures in an as-cast film also anisotropically guide dopants over substantial length scales. This phenomenon bears analogies to what occurs in block copolymer assemblies, where one block is mechanically strong and impermeable to dopant transport, which has also been demonstrated with SPT studies.<sup>53</sup> Whereas block copolymer applications make use of two different polymer components that must be carefully synthesized, here we suggest the possibility to take advantage of a single-component polymer with two different structural phases to achieve the same goal. To fully harness the potential of such an approach with a semicrystalline polymer, one could envision leveraging methods of controlled polymer or small organic molecule crystal growth<sup>65,66</sup> and taking inspiration from pre-existing strategies used for the directed self-assembly of block copolymers.<sup>67–69</sup>

**Conclusion.** Instead of relying on bulk approaches, we have directly measured strong correlations between nanoscale mobile probe dynamics obtained by SPT and the nanoscale microstructure of PEO thin films obtained by AFM. Specifically, we confirmed by direct measurement that particle, and potentially molecular, motion occurs preferentially, if not exclusively, in amorphous regions of the semicrystalline microstructure. The single-particle tracking that we employed affords not only these spatial correlations but also provides access to statistical distributions of the parameters associated with probe motion. Our correlated SPT and AFM phase imaging strategy could be readily adapted to study other semicrystalline polymers in order to learn how various crystalline and amorphous phases dictate transport in polymers known to have different melting or glass transition temperatures or other bulk properties. Future experiments could be performed to track ionic species or species sensitive to ions,<sup>70</sup> comparing the resulting dynamics to those measured with our hydrophobic fluorescent aggregates in this study. Differences between experiments employing charged and neutral probes could yield key insights to enable the deconvolution of size and charge in polymer–ion interactions important for ion diffusion in a solid-state electrolyte.

The strategies presented here could also be of great use in the study of impurity migration within materials composed of polymers quite different from the polymer electrolyte, for example, in plastics whose properties depend critically on eliminating impurities but where elimination strategies are neither systematic nor effective. Finally, our findings provide design principles to guide the current efforts for controlled crystalline domain growth in semicrystalline polymers. By arranging and aligning crystallites in an organized manner, the diffusion of dopants could be deterministically guided by bounded repeating arrays of crystalline and amorphous material.<sup>28</sup> This strategy would provide the necessary mechanical strength for device incorporation without compromising the transport of ions, drugs, and other dopants.

## ■ ASSOCIATED CONTENT

### Supporting Information

The Supporting Information is available free of charge at <https://pubs.acs.org/doi/10.1021/acs.jpcllett.0c01318>.

Materials and methods including sample preparation, widefield single-particle tracking setup, data analysis, spectrally resolved single-particle fluorescence setup; additional data, analysis, and characterization of fluorescent C6 probe complexes; additional random walk simulation results and analysis; additional AFM and SPT data for a variety of different sample conditions (PDF)

## ■ AUTHOR INFORMATION

### Corresponding Author

**Naomi S. Ginsberg** – Department of Chemistry, STROBE, National Science Foundation Science and Technology Center, and Department of Physics, University of California Berkeley, Berkeley, California 94720, United States; Materials Science Division and Molecular Biophysics and Integrated Bioimaging Division, Lawrence Berkeley National Laboratory, Berkeley, California 94720, United States; Kavli Energy NanoSciences Institute at Berkeley, Berkeley, California 94720, United States; [orcid.org/0000-0002-5660-3586](https://orcid.org/0000-0002-5660-3586); Email: [nsnginsberg@berkeley.edu](mailto:nsnginsberg@berkeley.edu)

### Authors

**Trevor D. Roberts** – Department of Chemistry, University of California Berkeley, Berkeley, California 94720, United States

**Rongfeng Yuan** – Department of Chemistry, University of California Berkeley, Berkeley, California 94720, United States; [orcid.org/0000-0002-6572-2472](https://orcid.org/0000-0002-6572-2472)

**Limin Xiang** – Department of Chemistry, University of California Berkeley, Berkeley, California 94720, United States

**Milan Delor** – Department of Chemistry, University of California Berkeley, Berkeley, California 94720, United States; [orcid.org/0000-0002-9480-9235](https://orcid.org/0000-0002-9480-9235)

**Ravi Pokhrel** – DuPont Electronics and Imaging, Marlborough, Massachusetts 01752, United States

**Ke Yang** – DuPont Electronics and Imaging, Marlborough, Massachusetts 01752, United States

**Emad Aqad** – DuPont Electronics and Imaging, Marlborough, Massachusetts 01752, United States

**Tomas Marangoni** – DuPont Electronics and Imaging, Marlborough, Massachusetts 01752, United States

**Peter Trefonas** – DuPont Electronics and Imaging, Marlborough, Massachusetts 01752, United States

**Ke Xu** – Department of Chemistry and STROBE, National Science Foundation Science and Technology Center, University of California Berkeley, Berkeley, California 94720, United States; [orcid.org/0000-0002-2788-194X](https://orcid.org/0000-0002-2788-194X)

Complete contact information is available at:

<https://pubs.acs.org/doi/10.1021/acs.jpcllett.0c01318>

### Author Contributions

<sup>#</sup>T.D.R. and R.Y. contributed equally to this work.

### Notes

The authors declare no competing financial interest.

## ■ ACKNOWLEDGMENTS

T.D.R., R.Y., and N.S.G. thank J. Raybin for assistance with phase AFM measurements. This work has been primarily

supported by DuPont Electronics and Imaging (formerly The Dow Chemical Company) through a University Partnership program under Contract No. 244699. Spectral localization microscopy was supported by STROBE, a National Science Foundation Science & Technology Center under Grant No. DMR 1548924. T.D.R. acknowledges a National Science Foundation Graduate Research Fellowship (DGE 1106400). N.S.G. acknowledges an Alfred P. Sloan Research Fellowship, a David and Lucile Packard Foundation Fellowship for Science and Engineering, and a Camille and Henry Dreyfus Teacher-Scholar Award.

## ■ REFERENCES

- (1) *Brydson's Plastics Materials*, 8th ed.; Gilbert, M., Ed.; Butterworth-Heinemann, 2017.
- (2) Bartczak, Z.; Argon, A. S.; Cohen, R. E.; Weinberg, M. Toughness Mechanism in Semi-Crystalline Polymer Blends: I. High-Density Polyethylene Toughened with Rubbers. *Polymer* **1999**, *40* (9), 2331–2346.
- (3) Mollinger, S. A.; Krajina, B. A.; Noriega, R.; Salles, A.; Spakowitz, A. J. Percolation, Tie-Molecules, and the Microstructural Determinants of Charge Transport in Semicrystalline Conjugated Polymers. *ACS Macro Lett.* **2015**, *4* (7), 708–712.
- (4) Pandey, A.; Toda, A.; Rastogi, S. Influence of Amorphous Component on Melting of Semicrystalline Polymers. *Macromolecules* **2011**, *44* (20), 8042–8055.
- (5) Jabbari-Farouji, S.; Rottler, J.; Lame, O.; Makke, A.; Perez, M.; Barrat, J.-L. Plastic Deformation Mechanisms of Semicrystalline and Amorphous Polymers. *ACS Macro Lett.* **2015**, *4* (2), 147–150.
- (6) Zhou, J.; Turner, S. A.; Brosnan, S. M.; Li, Q.; Carrillo, J.-M. Y.; Nykypanchuk, D.; Gang, O.; Ashby, V. S.; Dobrynin, A. V.; Sheiko, S. S. Shapeshifting: Reversible Shape Memory in Semicrystalline Elastomers. *Macromolecules* **2014**, *47* (5), 1768–1776.
- (7) Toolan, D. T. W.; Pullan, N.; Harvey, M. J.; Topham, P. D.; Howse, J. R. In Situ Studies of Phase Separation and Crystallization Directed by Marangoni Instabilities During Spin-Coating. *Adv. Mater.* **2013**, *25* (48), 7033–7037.
- (8) Sauer, B. B.; Hsiao, B. S. Effect of the Heterogeneous Distribution of Lamellar Stacks on Amorphous Relaxations in Semicrystalline Polymers. *Polymer* **1995**, *36* (13), 2553–2558.
- (9) Rastogi, S.; Lippits, D. R.; Peters, G. W. M.; Graf, R.; Yao, Y.; Spiess, H. W. Heterogeneity in Polymer Melts from Melting of Polymer Crystals. *Nat. Mater.* **2005**, *4* (8), 635–641.
- (10) Balani, K.; Verma, V.; Agarwal, A.; Narayan, R. Physical, Thermal, and Mechanical Properties of Polymers. *Biosurfaces: A Materials Science and Engineering Perspective* **2015**, 329–344.
- (11) Flory, P. J.; Yoon, D. Y. Molecular Morphology in Semicrystalline Polymers. *Nature* **1978**, *272*, 226–229.
- (12) Song, Y.; Feng, W.; Liu, K.; Yang, P.; Zhang, W.; Zhang, X. Exploring the Folding Pattern of a Polymer Chain in a Single Crystal by Combining Single-Molecule Force Spectroscopy and Steered Molecular Dynamics Simulations. *Langmuir* **2013**, *29* (12), 3853–3857.
- (13) Flory, P. J. On the Morphology of the Crystalline State in Polymers. *J. Am. Chem. Soc.* **1962**, *84* (15), 2857–2867.
- (14) Fullerton-Shirey, S. K.; Maranas, J. K. Effect of LiClO<sub>4</sub> on the Structure and Mobility of PEO-Based Solid Polymer Electrolytes. *Macromolecules* **2009**, *42* (6), 2142–2156.
- (15) Minier, M.; Berthier, C.; Gorecki, W. Thermal Analysis and NMR Study of a Poly(Ethylene Oxide) Complex Electrolyte: PEO(LiCF<sub>3</sub>SO<sub>3</sub>)<sub>x</sub>. *J. Phys. (Paris)* **1984**, *45* (4), 739–744.
- (16) Rhodes, C. P.; Frech, R. Local Structures in Crystalline and Amorphous Phases of Diglyme-LiCF<sub>3</sub>SO<sub>3</sub> and Poly(Ethylene Oxide)-LiCF<sub>3</sub>SO<sub>3</sub> Systems: Implications for the Mechanism of Ionic Transport. *Macromolecules* **2001**, *34* (8), 2660–2666.
- (17) Stoeva, Z.; Martin-Litas, I.; Staunton, E.; Andreev, Y. G.; Bruce, P. G. Ionic Conductivity in the Crystalline Polymer Electrolytes

PEO6:LiXF<sub>6</sub>, X = P, As, Sb. *J. Am. Chem. Soc.* **2003**, *125* (15), 4619–4626.

(18) Gadjourova, Z.; Martín y Marero, D.; Andersen, K. H.; Andreev, Y. G.; Bruce, P. G. Structures of the Polymer Electrolyte Complexes PEO6:LiXF<sub>6</sub> (X = P, Sb), Determined from Neutron Powder Diffraction Data. *Chem. Mater.* **2001**, *13* (4), 1282–1285.

(19) Zardalidis, G.; Ioannou, E.; Pispas, S.; Floudas, G. Relating Structure, Viscoelasticity, and Local Mobility to Conductivity in PEO/LiTf Electrolytes. *Macromolecules* **2013**, *46* (7), 2705–2714.

(20) Vallée, A.; Besner, S.; Prud'Homme, J. Comparative Study of Poly(Ethylene Oxide) Electrolytes Made with LiN(CF<sub>3</sub>SO<sub>2</sub>)<sub>2</sub>, LiCF<sub>3</sub>SO<sub>3</sub> and LiClO<sub>4</sub>: Thermal Properties and Conductivity Behaviour. *Electrochim. Acta* **1992**, *37* (9), 1579–1583.

(21) Li, X.; Cheng, S.; Zheng, Y.; Li, C. Y. Morphology Control in Semicrystalline Solid Polymer Electrolytes for Lithium Batteries. *Mol. Syst. Des. Eng.* **2019**, *4* (4), 793–803.

(22) Cheng, S.; Smith, D. M.; Li, C. Y. How Does Nanoscale Crystalline Structure Affect Ion Transport in Solid Polymer Electrolytes? *Macromolecules* **2014**, *47* (12), 3978–3986.

(23) Golodnitsky, D.; Strauss, E.; Peled, E.; Greenbaum, S. Review—On Order and Disorder in Polymer Electrolytes. *J. Electrochem. Soc.* **2015**, *162* (14), A2551–A2566.

(24) Sun, J.; Liao, X.; Minor, A. M.; Balsara, N. P.; Zuckermann, R. N. Morphology-Conductivity Relationship in Crystalline and Amorphous Sequence-Defined Peptoid Block Copolymer Electrolytes. *J. Am. Chem. Soc.* **2014**, *136* (42), 14990–14997.

(25) Xue, Z.; He, D.; Xie, X. Poly(Ethylene Oxide)-Based Electrolytes for Lithium-Ion Batteries. *J. Mater. Chem. A* **2015**, *3*, 19218–19253.

(26) Robitaille, C. D.; Fauteux, D. Phase Diagrams and Conductivity Characterization of Some PEO - LiX Electrolytes. *J. Electrochem. Soc.* **1986**, *133* (2), 315–325.

(27) Stolwijk, N. A.; Wieniczer, M.; Heddier, C.; Kösters, J. What Can We Learn from Ionic Conductivity Measurements in Polymer Electrolytes? A Case Study on Poly(Ethylene Oxide) (PEO)-NaI and PEO-LiTFSI. *J. Phys. Chem. B* **2012**, *116* (10), 3065–3074.

(28) Park, M. J. Confinement-Entitled Morphology and Ion Transport in Ion-Containing Polymers. *Mol. Syst. Des. Eng.* **2019**, *4* (2), 239–251.

(29) Croce, F.; Appetecchi, G. B.; Persi, L.; Scrosati, B. Nanocomposite Polymer Electrolytes for Lithium Batteries. *Nature* **1998**, *394* (6692), 456–458.

(30) Blümich, B.; Blümli, P. NMR Imaging of Polymer Materials. *Makromol. Chem.* **1993**, *194* (8), 2133–2161.

(31) McKenzie, I.; Harada, M.; Kiefl, R. F.; Levy, C. D. P.; MacFarlane, W. A.; Morris, G. D.; Ogata, S.-I.; Pearson, M. R.; Sugiyama, J.  $\beta$ -NMR Measurements of Lithium Ion Transport in Thin Films of Pure and Lithium-Salt-Doped Poly(Ethylene Oxide). *J. Am. Chem. Soc.* **2014**, *136* (22), 7833–7836.

(32) Klett, M.; Giesecke, M.; Nyman, A.; Hallberg, F.; Lindström, R. W.; Lindbergh, G.; Furó, I. Quantifying Mass Transport during Polarization in a Li Ion Battery Electrolyte by in Situ <sup>7</sup>Li NMR Imaging. *J. Am. Chem. Soc.* **2012**, *134* (36), 14654–14657.

(33) Frech, R.; Chintapalli, S.; Bruce, P. G.; Vincent, C. A. Crystalline and Amorphous Phases in the Poly(Ethylene Oxide)-LiCF<sub>3</sub>SO<sub>3</sub> System. *Macromolecules* **1999**, *32* (3), 808–813.

(34) Money, B. K.; Swenson, J. Dynamics of Poly(Ethylene Oxide) around Its Melting Temperature. *Macromolecules* **2013**, *46* (17), 6949–6954.

(35) Abbrent, S.; Greenbaum, S. Recent Progress in NMR Spectroscopy of Polymer Electrolytes for Lithium Batteries. *Curr. Opin. Colloid Interface Sci.* **2013**, *18* (3), 228–244.

(36) Bondia, P.; Casado, S.; Flors, C. Correlative Super-Resolution Fluorescence Imaging and Atomic Force Microscopy for the Characterization of Biological Samples. *Methods Mol. Biol.* **2017**, *1663*, 105–113.

(37) Beuwer, M. A.; Knopper, M. F.; Albertazzi, L.; van der Zwaag, D.; Ellenbroek, W. G.; Meijer, E. W.; Prins, M. W. J.; Zijlstra, P. Mechanical Properties of Single Supramolecular Polymers from

Correlative AFM and Fluorescence Microscopy. *Polym. Chem.* **2016**, *7* (47), 7260–7268.

(38) Cosentino, M.; Canale, C.; Bianchini, P.; Diaspro, A. AFM-STED Correlative Nanoscopy Reveals a Dark Side in Fluorescence Microscopy Imaging. *Sci. Adv.* **2019**, *5* (6), eaav8062.

(39) Marzantowicz, M.; Krok, F.; Dygas, J. R.; Florjańczyk, Z.; Zygadlo-Monikowska, E. The Influence of Phase Segregation on Properties of Semicrystalline PEO:LiTFSI Electrolytes. *Solid State Ionics* **2008**, *179* (27), 1670–1678.

(40) Fery-Forgues, S.; El-Ayoubi, R.; Lamère, J.-F. Fluorescent Microcrystals Obtained from Coumarin 6 Using the Reprecipitation Method. *J. Fluoresc.* **2008**, *18* (3–4), 619–624.

(41) Ghosh, P.; Das, T.; Maity, A.; Mondal, S.; Purkayastha, P. Incorporation of Coumarin 6 in Cyclodextrins: Microcrystals to Lamellar Composites. *RSC Adv.* **2015**, *5*, 4214–4218.

(42) Yan, R.; Moon, S.; Kenny, S. J.; Xu, K. Spectrally Resolved and Functional Super-Resolution Microscopy via Ultrahigh-Throughput Single-Molecule Spectroscopy. *Acc. Chem. Res.* **2018**, *51* (3), 697–705.

(43) Zhang, Z.; Kenny, S. J.; Hauser, M.; Li, W.; Xu, K. Ultrahigh-Throughput Single-Molecule Spectroscopy and Spectrally Resolved Super-Resolution Microscopy. *Nat. Methods* **2015**, *12* (10), 935–938.

(44) Corrent, S.; Hahn, P.; Pohlner, G.; Connolly, T. J.; Scaiano, J. C.; Fomes, V.; Garcia, H. Intrazeolite Photochemistry. 22. Acid-Base Properties of Coumarin 6. Characterization in Solution, the Solid State, and Incorporated into Supramolecular Systems. *J. Phys. Chem. B* **1998**, *102* (30), 5852–5858.

(45) Scaiano, J. C.; Laferriere, M.; Ivan, M. G.; Taylor, G. N. A Protocol for the Verification of Acid Generation in 157 Nm Lithography. *Macromolecules* **2003**, *36* (18), 6692–6694.

(46) Shen, H.; Tauzin, L. J.; Baiyasi, R.; Wang, W.; Moringo, N.; Shuang, B.; Landes, C. F. Single Particle Tracking: From Theory to Biophysical Applications. *Chem. Rev.* **2017**, *117* (11), 7331–7376.

(47) Kusumi, A.; Tsunoyama, T. A.; Hirose, K. M.; Kasai, R. S.; Fujiwara, T. K. Tracking Single Molecules at Work in Living Cells. *Nat. Chem. Biol.* **2014**, *10* (7), 524–532.

(48) Haas, B. L.; Matson, J. S.; DiRita, V. J.; Biteen, J. S. Single-Molecule Tracking in Live *Vibrio Cholerae* Reveals That ToxR Recruits the Membrane-Bound Virulence Regulator TcpP to the ToxT Promoter. *Mol. Microbiol.* **2015**, *96* (1), 4–13.

(49) Flier, B. M. I.; Baier, M. C.; Huber, J.; Müllen, K.; Mecking, S.; Zumbusch, A.; Wöll, D. Heterogeneous Diffusion in Thin Polymer Films As Observed by High-Temperature Single-Molecule Fluorescence Microscopy. *J. Am. Chem. Soc.* **2012**, *134* (1), 480–488.

(50) Bhattacharya, S.; Sharma, D. K.; Saurabh, S.; De, S.; Sain, A.; Nandi, A.; Chowdhury, A. Plasticization of Poly(Vinylpyrrolidone) Thin Films under Ambient Humidity: Insight from Single-Molecule Tracer Diffusion Dynamics. *J. Phys. Chem. B* **2013**, *117* (25), 7771–7782.

(51) Kastantin, M.; Keller, T. F.; Jandt, K. D.; Schwartz, D. K. Single-Molecule Tracking of Fibrinogen Dynamics on Nanostructured Poly(Ethylene) Films. *Adv. Funct. Mater.* **2012**, *22* (12), 2617–2623.

(52) Chen, R.; Li, L.; Zhao, J. Single Chain Diffusion of Poly(Ethylene Oxide) in Its Monolayers before and after Crystallization. *Langmuir* **2010**, *26* (8), 5951–5956.

(53) Tran-Ba, K.-H.; Higgins, D. A.; Ito, T. Fluorescence Recovery after Photobleaching and Single-Molecule Tracking Measurements of Anisotropic Diffusion within Identical Regions of a Cylinder-Forming Diblock Copolymer Film. *Anal. Chem.* **2015**, *87* (11), 5802–5809.

(54) Skaug, M. J.; Mabry, J. N.; Schwartz, D. K. Single-Molecule Tracking of Polymer Surface Diffusion. *J. Am. Chem. Soc.* **2014**, *136* (4), 1327–1332.

(55) Moerner, W. E.; Orrit, M. Illuminating Single Molecules in Condensed Matter. *Science* **1999**, *283* (5408), 1670–1676.

(56) Liao, Y.; Yang, S. K.; Koh, K.; Matzger, A. J.; Biteen, J. S. Heterogeneous Single-Molecule Diffusion in One-, Two-, and Three-Dimensional Microporous Coordination Polymers: Directional, Trapped, and Immobile Guests. *Nano Lett.* **2012**, *12*, 3080–3085.

- (57) Edelstein, A. D.; Tsuchida, M. A.; Amodaj, N.; Pinkard, H.; Vale, R. D.; Stuurman, N. Advanced Methods of Microscope Control Using Manager Software. *J. Biol. Methods* **2014**, *1* (2), 10.
- (58) Schindelin, J.; Arganda-Carreras, I.; Frise, E.; Kaynig, V.; Longair, M.; Pietzsch, T.; Preibisch, S.; Rueden, C.; Saalfeld, S.; Schmid, B.; et al. Fiji: An Open-Source Platform for Biological-Image Analysis. *Nat. Methods* **2012**, *9* (7), 676–682.
- (59) Li, L.; Chan, C.-M.; Yeung, K. L.; Li, J.-X.; Ng, K.-M.; Lei, Y. Direct Observation of Growth of Lamellae and Spherulites of a Semicrystalline Polymer by AFM. *Macromolecules* **2001**, *34* (2), 316–325.
- (60) Pearce, R.; Vancso, G. J. Imaging of Melting and Crystallization of Poly(Ethylene Oxide) in Real-Time by Hot-Stage Atomic Force Microscopy. *Macromolecules* **1997**, *30* (19), 5843–5848.
- (61) Beekmans, L. G. M.; van der Meer, D. W.; Vancso, G. J. Crystal Melting and Its Kinetics on Poly(Ethylene Oxide) by in Situ Atomic Force Microscopy. *Polymer* **2002**, *43* (6), 1887–1895.
- (62) Lei, Y.-G.; Chan, C.-M.; Li, J.-X.; Ng, K.-M.; Wang, Y.; Jiang, Y.; Li, L. The Birth of an Embryo and Development of the Founding Lamella of Spherulites As Observed by Atomic Force Microscopy. *Macromolecules* **2002**, *35* (18), 6751–6753.
- (63) McCulloch, I.; Heeney, M.; Bailey, C.; Genevicius, K.; MacDonald, I.; Shkunov, M.; Sparrowe, D.; Tierney, S.; Wagner, R.; Zhang, W.; et al. Liquid-Crystalline Semiconducting Polymers with High Charge-Carrier Mobility. *Nat. Mater.* **2006**, *5* (4), 328–333.
- (64) Noriega, R.; Rivnay, J.; Vandewal, K.; Koch, F. P. V.; Stingelin, N.; Smith, P.; Toney, M. F.; Salleo, A. A General Relationship between Disorder, Aggregation and Charge Transport in Conjugated Polymers. *Nat. Mater.* **2013**, *12* (11), 1038–1044.
- (65) Hu, Z.; Baralia, G.; Bayot, V.; Gohy, J.-F.; Jonas, A. M. Nanoscale Control of Polymer Crystallization by Nanoimprint Lithography. *Nano Lett.* **2005**, *5* (9), 1738–1743.
- (66) Bangsund, J. S.; Fielitz, T. R.; Steiner, T. J.; Shi, K.; Van Sambeek, J. R.; Clark, C. P.; Holmes, R. J. Formation of Aligned Periodic Patterns during the Crystallization of Organic Semiconductor Thin Films. *Nat. Mater.* **2019**, *18* (7), 725–731.
- (67) Raybin, J.; Ren, J.; Chen, X.; Gronheid, R.; Nealey, P. F.; Sibener, S. J. Real-Time Atomic Force Microscopy Imaging of Block Copolymer Directed Self Assembly. *Nano Lett.* **2017**, *17* (12), 7717–7723.
- (68) Mai, Y.; Eisenberg, A. Self-Assembly of Block Copolymers. *Chem. Soc. Rev.* **2012**, *41* (18), 5969–5985.
- (69) Song, J.-Q.; Liu, Y.-X.; Zhang, H.-D. Removal Pathways of Out-of-Plane Defects in Thin Films of Lamellar Forming Block Copolymers. *Macromolecules* **2018**, *51* (11), 4201–4212.
- (70) Padilla, N. A.; Rea, M. T.; Foy, M.; Upadhyay, S. P.; Desrochers, K. A.; Derus, T.; Knapper, K. A.; Hunter, N. H.; Wood, S.; Hinton, D. A.; et al. Tracking Lithium Ions via Widefield Fluorescence Microscopy for Battery Diagnostics. *ACS Sensors* **2017**, *2* (7), 903–908.